Accepted manuscript doi:
10.1680/jgeot.21.00068

Accepted manuscript
As a service to our authors and readers, we are putting peer-reviewed accepted manuscripts (AM) online, in the Ahead of Print section of each journal web page, shortly after acceptance.

Disclaimer
The AM is yet to be copyedited and formatted in journal house style but can still be read and referenced by quoting its unique reference number, the digital object identifier (DOI). Once the AM has been typeset, an 'uncorrected proof' PDF will replace the 'accepted manuscript' PDF. These formatted articles may still be corrected by the authors. During the Production process, errors may be discovered which could affect the content, and all legal disclaimers that apply to the journal relate to these versions also.

Version of record
The final edited article will be published in PDF and HTML and will contain all author corrections and is considered the version of record. Authors wishing to reference an article published Ahead of Print should quote its DOI. When an issue becomes available, queuing Ahead of Print articles will move to that issue's Table of Contents. When the article is published in a journal issue, the full reference should be cited in addition to the DOI.

Downloaded by [NORGES GEOTEKNISKE INSTITUTT] on [29/10/21]. Copyright © ICE Publishing, all rights reserved.

Accepted manuscript doi:
10.1680/jgeot.21.00068

Submitted: 22 April 2021

Published online in 'accepted manuscript' format: 03 August 2021

Manuscript title: Characteristics of cyclic undrained model SANISAND-MSu and their effects on response of monopiles for offshore wind structures

Authors: Haoyuan Liu* and Amir M. Kaynia*,†

Affiliations: *Norwegian Geotechnical Institute (NGI), Oslo, Norway and †Norwegian University of Science and Technology (NTNU), Trondheim, Norway

Corresponding author: Haoyuan Liu, Norwegian Geotechnical Institute (NGI), Oslo, Norway.

E-mail: haoyuan.liu@ngi.no

Downloaded by [NORGES GEOTEKNISKE INSTITUTT] on [29/10/21]. Copyright © ICE Publishing, all rights reserved.

Accepted manuscript doi:
10.1680/jgeot.21.00068

Abstract

Optimised design is essential to reduce the cost of monopiles for offshore wind turbines. For this purpose, an in-depth understanding of the behaviour of monopile-soil interaction is required. As more wind farms are planned in seismically active areas, the undrained behaviour of sandy soils (and possibility of soil liquefaction) and their effects on monopile cyclic response need a critical evaluation. Considering the lack of well-established test programs, implicit 3D Finite Element (FE) methods stand outas a robust tool to identify and highlight the governing geo-mechanisms in monopile design. In this work, an implicit 3D FE implementation of SANISAND-MS for undrained soil behaviour, termed SANISAND-MSu, is deployed in OpenSees to serve these objectives. The role of pore water pressure on monopile performance is comprehensively investigated by comparisons between drained and undrained soil behaviour. Local soil responses are studied in detail in relation to parameters in laboratory soil testing and application to monopile geotechnical design. The results of simulations are also used to evaluate numerical $p-y$ curves as function of number of load cycles on the pile. The conclusions in this work contribute to the ongoing research on monopile-soil interaction and support the development of lifetime analysis for monopile-soil systems.

Keywords: Numerical modelling; Sands; Piles & piling Soil/structure interaction; Pore pressures

Downloaded by [NORGES GEOTEKNISKE INSTITUTT] on [29/10/21]. Copyright © ICE Publishing, all rights reserved.

Accepted manuscript doi:
10.1680/jgeot.21.00068

Offshore wind energy has rapidly developed since the 1990s as one of the measures against greenhouse gas emissions. Currently, the dominant foundation type for offshore wind turbines (OWTs) is the monopile (Kaynia, 2019). Foundations for OWTs are exposed to harsh cyclic environmental loading induced by wind, wave and currents. At present, design of monopiles in industrial practise is largely based on load transfer curves (' $p-y$ ' curves) such as those recommended by the American Petroleum Institute (API, 2014). The $p-y$ formulations have their origins from the offshore oil and gas industry where flexible piles with relatively small diameters are used (DNV, 2016). As monopiles have generally much larger diameters, the adoption of non-optimized $p-y$ curves may lead to uneconomical, and possibly erroneous, design solutions (e.g., DNV (2016)). To reduce the uncertainty in design and achieve cost-efficient designs, it is essential to gain an in-depth understanding of the complex soil-structure interactions in OWT foundations especially for undrained soil response.

In spite of the commonly-adopted assumption of drained behaviour for saturated sand under long term cyclic loading events (e.g., API (2014)), monopile response in saturated sand is practically undrained during high-intensity cycles of most dynamic loads including seismic shaking (Esfeh & Kaynia, 2020; Kementzetzidis *et al*., 2020). The accumulated strain and pore water pressure in the soil due to environmental loads are relevant to all design criteria. This is due to the accompanying crucial change of thesoil stiffness and strength which in turn affect the structural dynamic response (Jostad *et al*., 2020). To critically evaluate the cyclic response of monopiles in saturated sand, an insight into the undrained soil response is necessary. Numerous studies including experimental work (LeBlanc *et al*., 2010; Truong *et al*., 2019; Abadie *et al*., 2019; Frick & Achmus, 2020) and numerical simulations (Jostad *et al*., 2014; Cuéllar *et al*., 2014; Tasiopoulou *et al*., 2021) have recently been performed to understand monopile response under cyclic loads. However, these studies are mostly limited to the dry sand or fully drained conditions.

Considering the lack of systematic experimental test results regarding the effects of pore water pressure (and possibly liquefaction of sand domain), the implicit step-by-step 3D FE analysis is believed to provide a means to reveal the links between global monopile response and local soil response (Liu *et al*., 2018; Ziotopoulou, 2018; Pisanó, 2019). The soundness of implicit 3D FE analysis depends highly on the constitutive modelling of the cyclic soil behaviour. Over the past decades, many constitutive models have been developed for such a purpose. Among those, bounding surface plasticity models are well recognised due to their satisfactory prediction ability. Specially, Dafalias & Manzari (2004) introduced fabric tensor in the flow rule to capture the realistic liquefaction triggering. The outcome model is referred to as SANISAND2004 in this work for brevity. Several variations of SANISAND have been proposed over the years (Petalas *et al*., 2019; Papadimitriou *et al*., 2019).

Recently, the memory enhanced SANISAND2004 model –SANISAND-MS, has been proposed and proven to be able to accurately predict sand ratcheting behaviour under various loading paths (Liu *et al*., 2019; Liu & Pisanó, 2019). Later, SANISAND-MS has been applied to boundary problems with focus on the cyclic monopile-soil interaction mechanisms in dry sand (Liu *et al*., 2021; Cheng *et al*., 2021). Satisfactory semi-quantitative comparison between the simulation and the experimental data from the literature (LeBlanc *et al*., 2010; Richards *et al*., 2020) has been obtained for the tilt accumulation of monopiles. From this, it is believed that SANISAND-MS in a 3D FE platform will give deeper insight into the controlling factors of cyclic hydro-mechanical behaviour of monopile. However, the original SANISAND-MS is believed to be less suitable for the simulation of undrained cyclic behaviour. Therefore, Liu *et al*. (2020) further improved SANISAND-MS for better simulation of undrained hydro-mechanical behaviour of sand. In this paper, the updated model is implemented in the

Downloaded by [NORGES GEOTEKNISKE INSTITUTT] on [29/10/21]. Copyright © ICE Publishing, all rights reserved.

Accepted manuscript doi:
10.1680/jgeot.21.00068

3D FE platform Open Sees and is referred to as SANISAND-MSu ('u' stands for undrained) to distinguish it from the original SANISAND-MS formulations.

Specially, SANISAND-MSu puts emphasis on the following aspects (Liu *et al*., 2020): (1) cycle-by-cycle pore pressure accumulation in pre-liquefaction regime (i.e., before the first-time effective stress approaches nearly zero); (2) strain accumulation in cyclic mobility (post-liquefaction) regime (but without losing the capability of reproducing sand ratcheting behaviour). SANISAND-MSu is implemented in this work for the first time for numerical simulations of cyclic hydro-mechanical behaviour of monopile foundation using an implicit 3D FE framework. This study aims to practically link local soil behaviour to global cyclic monopile response. It is believed that more rigorous 3D FE simulation enhanced by SANISAND-MSu can guide the soil testing program and optimise the OWT monopile design.

SANISAND-MSu model

Throughout this paper, tensor quantities are denoted in bold-face notations. Stress is indicated by $\boldsymbol{\sigma}$ (and are all effective in this work). Deviatoric stress $\boldsymbol{s} = \boldsymbol{\sigma} - p\boldsymbol{I}$, with $p = \left(\mathrm{tr}\boldsymbol{\sigma}\right)/3$ the average stress and $\boldsymbol{I}$ the identity matrix. The symbol *tr* represents the trace operator. The deviatoric stress ratio tensor $\boldsymbol{r} = \boldsymbol{s}/p$. $\varepsilon_{vol} = \mathrm{tr}\varepsilon$ is the volumetric strain. The superscripts e and p represent 'elastic' and 'plastic'.

SANISAND-MSu improves the original SANISAND-MS model by introducing the fabric history effects and stress ratio effects. The relevant loci of the model are given in Fig. 1a, which are: (1) a yield locus (f) defines the elastic region, (2) a bounding surface (f^B) encloses the admissible stress states; (3) a dilatancy locus (f^D) distinguishes the contractive and dilative soil behaviour and (4) a memory surface (f^M) phenomenologically captures the effect of soil fabric during the plastic straining. Detailed SANISAND-MSu formulation has been documented in Liu *et al*. (2020) and will not be presented in this paper. Instead, only the features related to the memory surface are briefly introduced.

The memory surface f^M tracks the increased hardening response and the stress-induced anisotropy through the evolution of its size m^M and center $\boldsymbol{\alpha}^M$. The evolution of f^M obeys two basic rules: (1) f^M evolves during plastic straining; (2) the memory surface always encloses the yield surface f.

The expansion of the memory surface (i.e., increase in m^M, denoted as dm_+^M) links the experimental observations of sand stiffening with reinforced fabric change under plastic contractive straining. On the contrary, dilative straining leads to an unstable (or a damage to) fabric configuration (Nemat-119 Nasser & Tobita, 1982) and is related to the shrinkage of the memory surface size (denoted as dm_-^M). The full evolution of the memory surface size dm^M is then defined as:

$$\begin{aligned} dm^M &= dm_+^M + dm_-^M \\ &= \sqrt{\frac{2}{3}} d\boldsymbol{\alpha}^M : \boldsymbol{n} + \frac{m^M}{\zeta} f_{shr} \left\langle b_r^d \right\rangle m_+^M \left\langle -d\varepsilon_{vol}^p \right\rangle \end{aligned} \tag{1}$$

where $d\boldsymbol{\alpha}^M$ denotes for the evolution of memory surface center (see Liu *et al*. 2020 for details). $\boldsymbol{n}$ is the unit deviatoric tensor normal to the yield locus. The term $m_+^M = \int dm_+^M$ represents for the fabric generation history. ζ is the memory shrinkage parameter and the function f_{shr} ensures that the yield surface is enclosed by the memory surface during

Downloaded by [NORGES GEOTEKNISKE INSTITUTT] on [29/10/21]. Copyright © ICE Publishing, all rights reserved.

Accepted manuscript doi:
10.1680/jgeot.21.00068

shrinking. To avoid the conflict in the changing of the memory surface size during strain softening, the shrinkage is terminated when $b_r^d = \left(\boldsymbol{\alpha}^b - \boldsymbol{\alpha}\right) : \boldsymbol{n} < 0$, $\boldsymbol{\alpha}^b$ is the image point of the yield surface center $\boldsymbol{\alpha}$ on the bounding surface f^B.

In SANISAND-MSu, the plastic deviatoric strain increment is the same as the definition in SANISAND2004 and will not be repeated here. The plastic volumetric strain increment $d\varepsilon_{vol}^p$ is defined via the dilatancy coefficient A_d. SANISAND-MSu enhanced A_d with new features including: (1) the fabric evolution history term F; (2) the ratio of mean effective stress p and the maximum ever-experienced mean effective stress p_{max}; (3) Lode angle (θ) effects and (4) piece-wise definition:

(1) $A_d = A_0$ when the soil is contractive ($d \geq 0$) and following previous contraction ($\tilde{b}_d^M \leq 0$).

$$A_d = A_0 \exp\left[\beta_1 F \left(\frac{p}{p_{max}}\right)^{0.5}\right] g^k(\theta) \tag{2}$$

(2) for current contraction ($d \geq 0$) but following previous dilative behaviour ($\tilde{b}_d^M > 0$).

$$A_d = A_0 \exp\left[\beta_2 F \left(1 - \left(\frac{p}{p_{max}}\right)^{0.5}\right) \frac{d}{\left\|\boldsymbol{\alpha}^c\right\|}\right] \frac{1}{g(\theta)} \tag{3}$$

(3) if current soil state is in dilative region ($d < 0$).

The term $d = \left(\boldsymbol{\alpha}^d - \boldsymbol{\alpha}\right) : n$ defines the relative position between the current stress sate and the phase transformation state. The term $\tilde{b}_d^M$ 'memorises' the soil contractive/dilative state in the previous strain increment. $\tilde{b}_d^M = \left(\tilde{\boldsymbol{\alpha}}^d - \tilde{\boldsymbol{r}}_\alpha^M\right) : \boldsymbol{n}$, with $\tilde{\boldsymbol{\alpha}}^d$ and $\tilde{r}_\alpha^M$ illustrated in Fig. 1b, and $\left\|\boldsymbol{\alpha}_c\right\|$ is the Euclidean norm of $\boldsymbol{\alpha}^c$ (the projection of $\boldsymbol{\alpha}$ on the critical surface f^C). Dilatancy parameters β_1 and β_2 govern the shear stain amplitude in post-dilation stage, and k is a model parameter. The term F is related to the fabric evolution history:

$$F = \ln\left[1 + \frac{\int dm_-^M}{\left(\int dm_+^M + \int dm_-^M\right)^{0.5}}\right] \tag{4}$$

The term F is a non-decreasing scalar. Thus, special evaluation is required when adopting SANISAND-MSu in the simulations involving distinct stages of consolidation.

In SANISAND-MSu, the current stress ratio $\eta = q / p = \sqrt{3} J_2$ is adopted in the hardening coefficient, with J_2 denoting the second invariant of the deviatoric stress tensor:

$$h = \frac{b_0}{\left(\boldsymbol{\alpha} - \boldsymbol{\alpha}_{in}\right) : \boldsymbol{n}} \exp\left[\mu_0 \left(\frac{p}{p_{atm}}\right)^{0.5} \left(\frac{b^M}{b_{ref}}\right)^{w_1} \frac{1}{\eta^{w_2}}\right] \tag{5}$$

where μ_0, w_1 and w_2 are model parameters and b^M represents the distance between $\boldsymbol{\alpha}$ and its projection $\boldsymbol{r}_\alpha^M$ on f^M.

Downloaded by [NORGES GEOTEKNISKE INSTITUTT] on [29/10/21]. Copyright © ICE Publishing, all rights reserved.

Accepted manuscript doi:
10.1680/jgeot.21.00068

Performance of SANISAND-MSu at soil element level

In this section, SANISAND-MSu is validated against cyclic tests on Karlsruhe fine sand, whose index properties are summarized as: maximum void ratio $e_{max} = 1.054$, minimum void ratio $e_{min} = 0.677$, uniformity coefficient $C_u = 1.5$, median particle diameter $D_{50} = 0.14$ mm. In addition, the modulus degradation and damping properties are compared with other literature data. The soil samples were prepared by air pluviation. The detailed calibration procedures are given in Liu *et al*. (2019, 2020) and will not be repeated here. The calibrated model parameters are summarized in Table 1.

Undrained cyclic DSS tests

Due to the lack of experimental data, only the comparisons between SANISAND-MSu and SANISAND2004 simulation results are made. SANISAND2004 takes no consideration of sand fabric effects in the pre-dilation regime. Hence, it overestimates the accumulated pore water pressure during each cycle. Moreover, no strain accumulation can be captured after only a few cycles in cyclic mobility regime (see Fig. 2a) – which disagrees with the experimental observations. The two limitations of SANISAND2004 are largely removed by the adoption of memory surface concept and piece-wise defined A_d in SANISAND-MSu, see Fig. 2b. The number of loading cycles to trigger initial liquefaction can be controlled by the memory-enhanced hardening coefficient h. Also, introduction of fabric history F into flow rule allows accumulation of strain in cyclic mobility regime. More realistic undrained cyclic response is obtained by SANISAND-MSu.

An interesting feature of SANISAND-MSu is that it is reduced to SANISAND2004 performance (i.e., excluding load-induced fabric effects) by setting the relevant model parameters. This is demonstrated by Fig. 2c, which shows almost the same responses as presented in Fig. 2a.

Undrained cyclic triaxial tests

Fig. 3 compares the SANISAND-MSu simulation results with the undrained cyclic triaxial test results. Detailed test/simulation conditions are indicated in the figure caption. As demonstrated in the figure, realistic progressive reduction of mean effective stress p is captured by SANISAND-MSu. Moreover, the accumulated strain level in cyclic mobility regime is comparable with the experimental data (Wichtmann & Triantafyllidis, 2016).

Fig. 4 presents the pore water pressure ratio r_u evolution against the number of loading cycles N. Here $r_u = 1 - \sigma_v / \sigma_{vo}$, with σ_{v0} indicates the initial vertical stress prior to the cyclic loading. The results suggest that SANISAND-MSu can accurately predict cycle-by-cycle pore water pressure accumulation for different loading conditions.

Stiffness degradation and damping ratio

In dynamic analyses of geo-structures, the variation of the soil stiffness/modulus and damping are important considerations to evaluate constitutive models. An effective way of assessing these features under cyclic loading is by the stiffness degradation (or modulus reduction, G / G_{max}) and damping (D) relationships with shear strain γ. These data are extensively used in nonlinear geotechnical analyses, especially for earthquake loading.

The results of simulations for drained and undrained monotonic triaxial tests were used to construct the modulus reduction curves for several values of initial effective vertical stress σ_{v0} (Fig. 5a) and relative density D_r (Fig. 5b). These results demonstrate that the larger the σ_{v0}, the larger the G / G_{max} at a given shear strain level. This agrees with the empirical predictions

Downloaded by [NORGES GEOTEKNISKE INSTITUTT] on [29/10/21]. Copyright © ICE Publishing, all rights reserved.

Accepted manuscript doi:
10.1680/jgeot.21.00068

proposed by Darendeli (2001). Whereas Sun *et al*. (1988) suggests σ_{v0} has no influence on G/G_{max} ratio. From the empirical conclusion, neither Darendeli (2001) nor Sun *et al*. (1988) suggest any direct considerations of the D_r on G/G_{max} ratio. For all cases, SANISAND-MSu predicts greater G/G_{max} ratios for the same shear strain level.

Damping ratio D is calculated from the ratio of the energy loss per cycle (ΔW) to the maximum stored energy (W), as defined in Eq. 6 and Fig. 6.

$$D = \frac{1}{4\pi}\frac{\Delta W}{W} \tag{6}$$

Fig. 7 compares the damping ratio generated by SANISAND-MSu for $N = 1$ together with the values using the empirical equations by Darendeli (2001) and those following the Masing rule. It is well-known that the Masing rule generates larger damping D at large strains γ. All the simulation results suggest that D first increase then decrease as γ increases. The decreasing of D is due to the dilative behaviour at large γ as presented in Fig. 2b. Such a tendency agrees with the experimental observations (Blaker & Andersen, 2019), but not captured by the empirical equation nor the Masing rule. There is no clear dependency of D on relative density D_r from the simulation results. This is in line with Darendeli's suggestion and Masing rule. The σ_{v0} level alters damping D in a way that D increases slightly with decreasing σ_{v0}, as indicated by Darendeli (2001) and SANISAND-MSu results (before the peak damping is reached).

Set up of the 3D FE model

Soil-monopile interaction is studied through an implicit 3D FE modelling approach. The FE platform OpenSEES was selected for implementation of the SANISAND-MSu model. In this section, the set-up of the 3D FE model is presented.

The 3D FE model is illustrated in Fig. 8, which consists of:

1. A tubular pile with diameter $D_{pile} = 5$ m, embedded length $L = 25$ m, wall thickness $t = 10$ cm. The dimension is comparable with a typical full-scale monopile.
2. A soil domain with length $w_s = 105$ m, width $w_d = 53$ m, depth $z_s = 48$ m. The geometry ratios ($w_s/2/D_{pile} = w_d/D_{pile} = 10.5$, $(z_s - L)/L = 0.92$) are considered large enough to avoid the boundary effects on the pile lateral response. The discussion in this work is limited to mono-directional lateral loading, only half of the entire soil domain was simulated due to the symmetry.
3. Symmetric sinusoidal load cycles were applied at the pile head which was taken at the level of soil surface, for non-linear static simulation. The initial loading direction as indicated in Fig. 8 (H). Such kind of loading is not realistic for an OWT due to zero eccentricity ratio $e_{ecc}/L = 0$. Nevertheless, the objective of this work is to assess: (1) the performance of SANISAND-MSu in a practical design and (2) the impact of the undrained soil behaviour on the global pile response due to cyclic loading – the eccentricity does not affect such a purpose.

The bottom boundary of the soil is fixed in all dimensions and the upper surface is free. The horizontal displacement is restrained on the surface perpendicular to the lateral surface. Drainage is only allowed at the top surface. SANISAND-MSu formulationswere integrated at the stress points through the fourth-order explicit Runge-Kutta method (Sloan, 1987). The soil domain was assumed uniform Karlsruhe fine sand with $D_r = 80\%$ (which is close to the

Downloaded by [NORGES GEOTEKNISKE INSTITUTT] on [29/10/21]. Copyright © ICE Publishing, all rights reserved.

Accepted manuscript doi:
10.1680/jgeot.21.00068

'dense' state in sandy wind farms) and was simulated with SANISAND-MSu. The pile-soil interface (10 cm thickness) was simulated using the same model but 'degraded' G_0 parameter (G_0 is a dimensionless model constant; $G_0 = 70$ was used for the interface layer). SANISAND-MSu is made to track the load-induced soil fabric effects on soil cyclic behaviour through the 'memory surface'. However, for simplicity, the initial memory surface size and location were set to coincide with those of the yield surface. Careful considerations are required if pile installation effects need to be highlighted.

In cyclic simulation cases, the number of loading cycles is limited to $N = 10$, which is a good representation of earthquake loading (Kramer *et al*., 1996). Two different kinds of simulations were performed: simulation in fully undrained sand domain (realised by setting permeability of soil domain as 10^{-10} m/s) and simulation in fully drained sand domain (permeability equals to 10^{10} m/s). For a direct comparison, other parameters and loading conditions were kept the same for the fully undrained and fully drained soil domains.

Simulation of monopile response

In this section, 3D FE simulation results are investigated to verify the SANISAND-MSu performance in real boundary value problems including pore water pressure effects. The simulation results are further evaluated to highlight the difference of global monopile behaviour between fully drained and undrained conditions and to understand the effect of pore water pressure on cyclic behaviour of large monopiles. Since the primary focus of this study has been on the cyclic response, the performance of SANISAND-MSu on reproducing the monotonic response of monopiles is not included.

Features of first loading cycle

In an initially homogeneous sand domain, monopile response under symmetric loading cycles is conventionally considered as symmetrical and close-ended force-displacement loops are assumed for this situation. Such a simplification was considered as realistic (at least for the dry soil domain) and is adopted for empirical equations so that under symmetric loading conditions, no displacement will be accumulated (e.g., LeBlanc *et al*. (2010)). However, recent centrifuge tests by Richards *et al*. (2021) on dry sand domain clearly show the asymmetric behaviour and obvious accumulation of pile-head displacement even after the first loading cycle (see Fig. 9a, where H_{ref} denotes the monotonic lateral load to trigger pile lateral deflection of $0\hat{A}\cdot1D_{pile}$ at the ground surface), especially for the test performed under 80g which is close to prototype test. This is confirmed by both SANISAND-MSu and SANISAND2004 models, based on the observations made from Fig. 9b:

1. for drained sand, the non-closed force-displacement loops are simulated, which result in an accumulation of pile head displacement on the side opposite to the initial loading direction. Such non-closed loops are believed to be due to the inhomogeneity induced by the first monotonic (virgin) loading up to the maximum load in the initially homogeneous soil (see the discussion in the following section for subsequent load cycles). It also suggests that the foundation system behaves stiffer in reloading path than in unloading path.
2. for undrained sand, almost a close-ended force displacement loop is formed. The load induced anisotropy is less obvious than the drained case.

When comparing SANISAND-MSu results with SANISAND2004 results, SANISAND2004 predicts larger pile-head displacement for the first loading cycle (Fig. 9b). This is because SANISAND2004 only considers the inherent fabric effects (soil fabric formed prior to

Downloaded by [NORGES GEOTEKNISKE INSTITUTT] on [29/10/21]. Copyright © ICE Publishing, all rights reserved.

Accepted manuscript doi:
10.1680/jgeot.21.00068

loading), while SANISAND-MSu also includes the load-induced fabric enhancement on sand stiffness.

Stress redistribution during loading cycles and the consequence of sand fabric evolution may be attributed to this 'load-induced asymmetry'. To demonstrate this mechanism, the distribution of the p / p_{in} ratio in the entire soil domain for $N = 1$ is presented in Figs. 10a - 10d, where p_{in} is the effective confining pressure after consolidation. Figs. 10e - 10f present the p / p_{in} ratio at $N = 10$ and will be discussed in the following section together with the discussion on the pore water pressure distribution.

Cyclic loading in FE simulation is applied first from right to left as indicated in Fig. 8 by H. Two characteristic states, namely C_A with $H = H_{max}$ for the first time and C_B at the end of the first loading cycle ($H = 0$) are studied. For characteristic state C_A, the drained simulation clearly shows the increasing p / p_{in} at the loading direction (Fig. 10b), while for the undrained case (Fig. 10a), such kind of unbalanced p / p_{in} distribution is less obvious.

This is also true in the characteristic state C_B for the undrained case (Fig. 10c) where p / p_{in} decreases for the affected soil zone (which lies symmetrically at the shallow surface around pile). While under drained condition, increasing of p / p_{in} is observed at the shallow surface (and more significant at the right corner to the pile) and slight decreasing of p / p_{in} is captured at the deeper layers (Fig. 10d). Stress redistribution can lead to the decrease in confining pressure even in drained soil (i.e., not due to pore water pressure accumulation). This effect was first observed numerically by Liu *et al*. (2021).

Pile response during loading cycles

Fig. 11 shows the evolution of pile-head force-displacement with load cycles. Both the simulations for undrained sand and drained sand are included. There is an apparent net pile-head displacement accumulation observed during the undrained case in each cycle (Fig. 11a). Despite the slightly non-symmetric behaviour for the first loop, the force-displacement loops in undrained case present progressive softening pile response with loading cycles. Pile-head displacement evolves rapidly with loading cycles and show increasing non-linear pattern. This can be attributed to three reasons: (1) the dissipation of fabric effects: the large pore water pressure promotes the sand entering dilative soil zone and accelerate the destroy of load induced fabric – which is captured by the memory surface evolution in SANISAND-MSu (the decrease of memory surface size leads to the reduction of sand stiffness reinforcement); (2) the reduction of confining pressure (as the combining effects of pore water pressure accumulation and stress redistribution) decreases soil stiffness; (3) sand stiffening in undrained case benefited from particle redistribution (phenomenologically captured through memory surface features) is less obvious compared to the drained case. Reduction of the confining pressure in undrained simulation is shown in Fig. 10e and can be compared with the pore water pressure distribution as indicated in Fig. 12.

For drained case, as illustrated in Fig. 11b, the maximum pile head displacement decreases from $\sim 0.7m$ for $N = 1$ to $\sim 0.5m$ for $N = 2$. This is due to the soil inhomogeneity caused by the initial loading (consistent with the experimental observation as described earlier in relation to Fig. 9). For $N \geq 3$, the maximum pile head displacement keeps increasing. The effect of inhomogeneity during these cycles is reduced due to the subsequent loading of the soil on both sides of the pile.

Downloaded by [NORGES GEOTEKNISKE INSTITUTT] on [29/10/21]. Copyright © ICE Publishing, all rights reserved.

Accepted manuscript doi:
10.1680/jgeot.21.00068

Fig. 12 shows that the pore water pressure presents symmetrical wedge-type distribution around the monopile. The highest pore water pressure is accumulated at pile tip. It should be noticed that there is also negative pore water pressure generated slightly below the pile tip. In the zone almost identical to the pore water pressure distribution 'wedge', small p / p_{in} ratio is generated in undrained simulation (see Fig. 10e). The p / p_{in} ratio distribution in drained (Fig. 10f)and undrained (Fig. 10e) simulations at the end of the $N = 10$ are different in several respects. Simulation of pile behaviour in dry sand domain from Liu *et al*. (2021) demonstrates that reduction in stress ratio p / p_{in} occurs due to stress redistribution even without pore water pressure generation. Same conclusion is drawn here in the saturated soil domain but under drained condition (Fig. 10f). Such a reduction of p / p_{in} in drained condition is less obvious than that in the undrained case. In summary, the dominated cause of such a reduction is the generation of pore water pressure under undrained situation. To quantitatively compare the reduction, the zone with $p / p_{in} < 0.2$ is highlighted in Fig. 10e and 10f. In undrained simulation: (1) almost the entire wedged zone is characterised with $p / p_{in} < 0.2$; (2) there is barely any increase in p / p_{in} in the entire soil domain (except the small areas close to pile shaft at very shallow depth). These are in contrast with the observations in drained case, where: (1) the small p / p_{in} (< 0.2) zones lie at the edge of the wedge zone, far from pile shaft above the pile rotation level; (2) there is a clear increase in p / p_{in} at far field zones and around the pile tip. These differences lead to stiffer foundation behaviour at relatively large load cycles and results in much smaller pile head displacement accumulation in drained case.

In the undrained case under identical conditions, the p / p_{in} ratio show significant difference in value and distribution from drained case. The reason is that in the undrained soil, the accumulated pore water pressure dominates the behaviour. Relatively high pore water pressure promotes dense sand entering the dilative regime that causes the unstable fabric configuration in the following contractive regime, while for drained case, particle reorganisation is a non-negligible source of fabric reinforcement. Effects of load-induced asymmetry and importance of drainage condition (pore pressure effects) need to be evaluated for more accurate pile displacement predictions.

Fig. 13 displays the evolution of pile deformation at $H = H_{max}$ with loading cycles. In addition to different pile-head displacements in different drainage conditions (as discussed in Fig. 11), there is also a difference in the locations of pile rotation points. The rotation point for the undrained case occurs at $\sim 0.85L$ (21.3m, see Fig. 13a) in depth, which is deeper than 19.5m ($\sim 0.78L$) in the drained simulation (Fig. 13b). This might be attributed to the more significant p reduction around the rotation point for undrained case. Another observation that deserves attention is the deformation of the pile body. For all N in drained case and $N = 1$ in undrained case, there is an obvious curvature in the pile deformation. However, as N increases in undrained case, the pile rotates closer to 'rigid' type which indicated reduced bending moment in the pile.

Fig. 14 presents the variation of the simulated lateral soil reaction (total force in case of undrained condition) of the pile (solid lines with markers) at $H = H_{max}$ for $N = 1$, 4, 7 and 10 cycles for both the undrained (Fig.14a) and drained (Fig. 14b) soil conditions. Similar pile reaction profile is obtained for drained and undrained cases for $N = 1$. Thus, before any substantial pore water pressures are generated, the lateral soil reaction is hardly affected by the drainage condition. For $N > 1$, the magnitude of the reaction force at shallow depths (

Downloaded by [NORGES GEOTEKNISKE INSTITUTT] on [29/10/21]. Copyright © ICE Publishing, all rights reserved.

Accepted manuscript doi:
10.1680/jgeot.21.00068

$z=[-4.5, 0]$ m) increases significantly with loading cycles for the undrained case. The obvious increase in soil reaction force with loading cycles can be due to the strong dilative soil behaviour (i.e., gaining strength) in the undrained case in the soil zones near the pile at shallow depth. Below $z=-4.5$ m, the lateral soil reaction decreases in magnitude with increasing N. Also, for all N, larger reaction force is activated at deeper soil layers. For drained case, the shape of the reaction curves has only a slight change during the first 10 cycles (Fig. 14b).

For both undrained and drained cases, the profiles of reaction force obtained by ignoring the inner soil contribution (dash lines) are included in Fig. 14 for $N=10$. Above the pile rotation point, the contribution from inner soil can be neglected (solid lines are almost identical with the dash lines). However, significant differences are observed below the rotation points. When neglecting inner soil contribution, the calculated reaction force at pile tip can be 30% less for the undrained case and 40% less for the drained case. Therefore, at deeper layers, the soil inner soil resistance should not be ignored.

Using the lateral pile reactions, one can compute the shear forces (Figs. 15a - 15b) and bending moments (Figs. 15c - 15d) along the pile at $H=H_{max}$ for $N=1$, 4, 7 and 10. The shear force decreases from mud-line to $\sim 3D_{pile}$ (for undrained case, Fig. 15a) depth and $\sim 2.5D_{pile}$ (for drained case, Fig. 15b) and then increases with the opposite sign until the rotation point. Below the rotation point, the shear force decreases again. For $N=1$, the shear force distribution for undrained and drained case are almost the same. After the first cycle, the magnitude of shear force decreases with loading cycles for the undrained case (Fig. 15a). While for the drained case, almost identical shear force profiles are obtained for all loading cycles (Fig. 15b).

For the undrained case, the bending moment at all depths increase for $N=1\sim 4$ and then decrease for $N>4$ (Fig. 15c). For drained case, the bending moment decreases as N increases due to the softening of the soil (although the variations are small for $N>1$, see Fig. 15d).

The computed cyclic $p-y$ relationships at two representative depth, namely 1.5 m ($\sim 0.3D_{pile}$) and 12.5 m ($\sim 2.5D_{pile}$) are presented in Fig. 16. For the undrained case, soil resistance keep increasing for $z=0.3D_{pile}$, possibly due to the easy triggering of soil dilative behaviour in shallow soil depth, together with the balance between the load-induced fabric reinforcement and soil degradation caused by pore water pressure generation. For $z=2.5D_{pile}$, dilative soil behaviour is more difficult to be triggered: soil resistance first increases (up to $N=3$) then decreases. For the drained case, the cyclic $p-y$ relationships after $N=2$ exhibits no significant variations with load cycles.

Responses of representative soil elements

The results of 3D FE analysis enhanced by an implicit constitutive model are believed to shed light on the understanding of local soil behaviour around monopile. In this section, the response of the representative elements (locations as marked in Fig. 8) are investigated in detail. Such information is potentially giving insights into the optimization of monopile design from the lab testing perspective.

Downloaded by [NORGES GEOTEKNISKE INSTITUTT] on [29/10/21]. Copyright © ICE Publishing, all rights reserved.

Accepted manuscript doi:
10.1680/jgeot.21.00068

Fig. 17 presents the stress paths in the $\frac{\tau_{xz}}{p} \sim \frac{\sigma_z - \sigma_x}{2p}$ plane (i.e., similar to the discussion in Cheng *et al*. 2021), where σ_z and σ_x are the vertical and horizontal stress, respectively; τ_{xz} is the shear stress applied perpendicular to x direction, along z direction. The color indicates the number of loading cycles (as denoted by the side color bars).

Element A lies at about $1D_{pile}$ in depth and $0.25 \sim 0.5D_{pile}$ near the pile shaft on the fore side of the pile; element C lies on the rear side of the pile at the same depth and distance from the pile. Starting from the positive $\frac{ma_z - \sigma_x}{2p}$, the stress path of Element A (Fig. 17a) moves towards negative side during the loading path at $N = 1$. As N increases, the inclination of the stress loop increases â€“ the stress state progressively evolves towards pure shear state. Also, the magnitude of the shear stress ratio $\frac{\tau_{xz}}{p}$ increases with increasing N. A nearly symmetrical behaviour is observed at element C, especially when $N > 2$ (Fig. 17c). The asymmetrical stress paths for elements A and C during $N = 1$ (and the quick transition into symmetrical stress paths afterwards) provide evidence to the observations regarding the discussion on pile head response (Fig. 9 to Fig. 11) from local soil element level.

For the element B located at the same depth but further away from the pile shaft ($1.2 \sim 1.5D_{pile}$), the stress path evolves in triaxial type for $N \leq 4$ (i.e., evolves back-and-forth along the $\frac{\sigma_z - \sigma_x}{2p}$ axis, see Fig. 17b).For larger N, more pronounced non-linear behaviour is observed, with larger shear response being mobilised, but still around the $\frac{\sigma_z - \sigma_x}{2p}$ axis, and smaller in magnitude compare to element A response.

Element D lies beneath element A at a depth $\sim 2.5D_{pile}$ below mud-line. The response of element D is similar to the responses of element A and C, except for the smaller variations in magnitude during stress path evolution (Fig. 17d).

The evolution in stress paths for the representative elements A, B, C and D indicate that the soil-to-pile distance has greater effects (compared to the depth of soil elements) on stress path variation in undrained sand. This is contrary to the conclusion from dry sand simulations (Cheng *et al*., 2021). Evolution of soil stress paths and the inclination of the stress loop in soil elements around monopiles correspond to a rotation of principal stress axes, which cannot be captured by conventional triaxial or DSS tests. More advanced test methods, such as hollow-cylinder torsional apparatus (HCTA) tests can serve for such a purpose, with the input stress path obtained from implicit 3D FE analysis.

The $q \sim p$ and $\tau \sim \gamma$ responses of the representative elements are presented in Fig. 18, with the colour indicating the evolution of lode angle (defined within $\left[0^\circ, 60^\circ\right]$, where 0° represents triaxial compression and 60° corresponds to triaxial extension). Clear transition from triaxial compression to triaxial extension is observed for almost all elements at all N. This, as already mentioned, is due to the simultaneous variation of the normal and shear stresses in each cycle.

Downloaded by [NORGES GEOTEKNISKE INSTITUTT] on [29/10/21]. Copyright © ICE Publishing, all rights reserved.

Accepted manuscript doi:
10.1680/jgeot.21.00068

Regarding the strain evolution ($\tau \sim \gamma$ plots in Fig. 18), the double-amplitude shear strain evolves during cycles, as a direct consequence of the modified dilatancy coefficient A_d adopted in SANISAND-MSu model. Despite ofthe continuous variation of Lode angle within each cycle (especially after the second cycle), the significant increase in the strain level occurs at Lode angles around 0° and 60° for all elements. This might contribute to the estimation of the accumulated pile displacement in the real design when significant pore water pressure is generated in the soil.

Fig. 19 compares the evolution of pore water pressure ratio under different cyclic loading levels. Despite the occurrence of large pore water pressure at larger depth, the shallower soil elements experience more rapid r_u increasing with loading cycles (compare response of element A and D). For elements symmetrically located on the different sides of the pile (element A and C), the evolution of r_u shows almost the same pattern. As expected, the element located further fromthe pile shaft experiences slower increase of r_u. For smaller cyclic loads (Fig. 19a, only half load in Fig. 19a is applied), the soil elements at shallow layer are less likely to approach liquefaction.

Conclusion remarks

In this work, the features of SANISAND-MSu are first discussed through triaxial and DSS test simulation results. Model performances on the prediction of variation of the soil modulus and damping are studied by comparing with empirical results.

Monopile cyclic hydro-mechanical behaviour has been studied through SANISAND-MSu enhanced implicit 3D FE modelling approach. The role of pore water pressure is highlighted through comparisons between the drained and undrained simulation results in fully saturated dense sand domains. Variation of distributions of reaction force and bending moment under different drainage conditions are discussed. Evolution of cyclic '$p-y$' curves are presented for both drained and undrained simulations. Responses of soil elements around monopile are evaluated to inform laboratory soil element tests in support of optimised offshore foundation designs.

The results in this work contribute to more in-depth and rigorous understanding of soil-structure interaction mechanisms in monopile foundation and motivates the use of implicit 3D FE method in evaluating OWTs monopile design choices. The selection of SANISAND-MSu model is quite natural for future seismic soil-foundation interaction analyses of offshore foundations.

Notation

A_0	'intrinsic' dilatancy parameter
A_d	Dilatancy coefficient
b_0	Hardening factor
$\tilde{b}_d^M$	Distance factor reflects the soil contractive/dilative state in the previous strain increment
b^M	Yield-to-memory surface distance
b_r^d	Relative distance between the yield surface centre and its image point on the bounding surface
b_{ref}	reference distance for normalisation
c_h	Hardening parameter
C_u	Uniformity coefficient
c_z	Fabric parameter in SANISAND2004

Downloaded by [NORGES GEOTEKNISKE INSTITUTT] on [29/10/21]. Copyright © ICE Publishing, all rights reserved.

Accepted manuscript doi:
10.1680/jgeot.21.00068

D_{50}	diameter in the particle-size distribution curve corresponding to 50% finer
dm_{+}^{M}	Increase of the memory surface size
dm_{-}^{M}	Shrinkage of the memory surface size
D_{pile}	Diameter of the monopile
e_0	Reference critical void ratio
e_{ecc}	Load eccentricity
$e_{max,min}$	The maximum and minimum void ratio
$f^{B,C,D}$	Bounding, critical, dilatancy surface function
f_{shr}	Memory surface shrinkage geometrical factor
f^{M}	Memory function
G_0	Dimensionless shear modulus
G_{max}	Maximum shear modulus
h_0	Hardening parameter
H_{ref}	H value corresponds with a pile lateral deflection of $0.1D_{pile}$ at the ground surface
m^{M}	Memory loci opening parameter
$n^{b,d}$	State parameter dependence parameters
p_{atm}	Atmospheric pressure
p_{in}	Initial effective mean stress
p_{max}	The maximum ever-experienced mean effective stress
q^{ampl}	Cyclic deviatoric stress amplitude
r_u	Pore water pressure ratio
$w_{1,2}$	Model hardening parameters
$w_{s,d}$	Length and width of the soil domain
z_{max}	Fabric parameter in SANISAND2004
z_s	Soil depth
$\beta_{1,2}$	Dilatancy parameters
$\beta_{1,2}$	dilatancy memory parameters
ε_{vol}	Volumetric strain
λ_c	Critical state line shape parameter
μ_0	Ratcheting parameter
σ_v	Vertical stress
σ_{v0}	Initial vertical stress
σ_x	Horizontal stress
τ^{ampl}	Cyclic shear stress amplitude
τ_{xz}	Shear stress applied perpendicular to x direction, along z direction
$\boldsymbol{\alpha}^{b,c,d}$	Image back-stress ratios on bounding, critical and dilatancy surface
$\boldsymbol{\alpha}_{in}$	Back-stress ratio at the starting point or upon load increment reversals
$\boldsymbol{\alpha}^{M}$	Centre of memory surface
c	Compression-to-extension strength ratio
d	The relative position between the current stress state and the phase transformation state
D	Damping
f	Yield function
F	Fabric evolution history term
G	Shear modulus

Downloaded by [NORGES GEOTEKNISKE INSTITUTT] on [29/10/21]. Copyright © ICE Publishing, all rights reserved.

Accepted manuscript doi:
10.1680/jgeot.21.00068

$g(\theta)$	Interpolation function for Lode angle dependence
h	Hardening factor
H	Horizontal load
k	Model hardening parameter
L	Embedded pile length
M	Critical stress ratio in compression
N	Number of loading cycles
p	Effective mean stress
t	Thickness of the shell of the monopile
W	The maximum stored energy
γ	Shear strain
Δu	Excess pore water pressure ratio
ΔW	The energy loss per load cycle
ζ	Memory surface shrinkage parameter
ζ	Memory surface shrinkage parameter
η	Current stress ratio
θ	Lode angle
ν	Poisson ratio
ξ	Critical state line shape parameter
τ	Shear stress
$\mathbf{n}$	Unit tensor normal to the yield locu
$\mathbf{s}$	Deviatoric stress tensor
$\boldsymbol{I}$	Second-order identity tensor
$\boldsymbol{\varepsilon}$	Strain tensor
$\boldsymbol{\sigma}$	Effective stress tensor
$\tilde{\boldsymbol{r}}_{\alpha}^{M}$	Projection of $\boldsymbol{\alpha}$ on the memory surface along $-\mathbf{n}$
$\tilde{\boldsymbol{\alpha}}^{d}$	Projection of $\boldsymbol{\alpha}$ on the dilatancy surface along $-\mathbf{n}$

References

Abadie, C. N., Byrne, B. W. & Houlsby, G. T. (2019). Rigid pile response to cyclic lateral loading: laboratory tests. *Géotechnique* **69**, No. 10, 863–876.

API (2014). *Recommended practice 2AWSD planning, designing and constructing fixed offshore platforms â€“working stress design, 22nd edn.* American Petroleum Institute.

Blaker, Ø. & Andersen, K. H. (2019). Cyclic properties of dense to very dense silica sand. *Soils and Foundations* **59**, No. 4, 982–1000.

Cheng, X. Y., Diambra, A., Ibraim, E., Liu, H. Y. & Pisanò, F. (2021). 3D FE-informed laboratory soil testing for the design of offshore wind turbine monopiles. *Journal of Marine Science and Engineering* **9**, No. 1, 101.

Cuéllar, P., Mira, P., Pastor, M., Merodo, J. A. F., Baeßler, M. & Rücker, W. (2014). A numerical model for the transient analysis of offshore foundations under cyclic loading. *Computers and Geotechnics* **59**, 75–86.

Dafalias, Y. F. & Manzari, M. T. (2004). Simple plasticity sand model accounting for fabric change effects. *Journal of Engineering mechanics* **130**, No. 6, 622–634.

Darendeli, M. B. (2001). *Development of a new family of normalized modulus reduction and material damping curves*. Ph.D. thesis, The University of Texas at Austin.

Downloaded by [NORGES GEOTEKNISKE INSTITUTT] on [29/10/21]. Copyright © ICE Publishing, all rights reserved.

Accepted manuscript doi:
10.1680/jgeot.21.00068

DNV (2016). DNVGL-ST-0126: Support structures for wind turbines. *Oslo, Norway: DNV GL* .

Esfeh, P. K. & Kaynia, A. M. (2020). Earthquake response of monopiles and caissons for offshore wind turbines founded in liquefiable soil. *Soil Dynamics and Earthquake Engineering* **136**, 106213.

Frick, D. & Achmus, M. (2020). An experimental study on the parameters affecting the cyclic lateral response of monopiles for offshore wind turbines in sand. *Soils and Foundations* **60**, No. 6, 1570–1587.

Jostad, H., Grimstad, G., Andersen, K., Saue, M., Shin, Y. & You, D. (2014). A FE procedure for foundation design of offshore structures–applied to study a potential owt monopile foundation in the korean western sea. *Geotechnical Engineering Journal of the SEAGS & AGSSEA* **45**, No. 4, 63–72.

Jostad, H. P., Dahl, B. M., Page, A., Sivasithamparam, N. & Sturm, H. (2020). Evaluation of soil models for improved design of offshore wind turbine foundations in dense sand. *Géotechnique* , 1–18.

Kaynia, A. M. (2019). Seismic considerations in design of offshore wind turbines. *Soil Dynamics and Earthquake Engineering* **124**, 399–407.

Kementzetzidis, E., Metrikine, A. V., Versteijlen, W. G. & Pisanò, F. (2020). Frequency effects in the dynamic lateral stiffness of monopiles in sand: insight from field tests and 3d fe modelling. *Géotechnique* , 1–14.

Kramer, S. L. *et al.* (1996). *Geotechnical earthquake engineering*. Pearson Education India.

LeBlanc, C., Houlsby, G. T. & Byrne, B. W. (2010). Response of stiff piles in sand to long-term cyclic lateral loading. *Géotechnique* **60**, No. 2, 79–90.

Liu, H. Y., Abell, J. A., Diambra, A. & Pisanò, F. (2019). Modelling the cyclic ratcheting of sands through memory-enhanced bounding surface plasticity. *Géotechnique* **69**, No. 9, 783–800.

Liu, H. Y., Diambra, A., Abell, J. A. & Pisanò, F. (2020). Memory-enhanced plasticity modeling of sand behavior under undrained cyclic loading. *Journal of Geotechnical and Geoenvironmental Engineering* **146**, No. 11, 04020122.

Liu, H. Y., Kementzetzidis, E., Abell, J. A. & Pisanò, F. (2021). From cyclic sand ratcheting to tilt accumulation of offshore monopiles: 3D FE modelling using sanisand-ms. *Géotechnique* , 1–45.

Liu, H. Y. & Pisanò, F. (2019). Prediction of oedometer terminal densities through a memory-enhanced cyclic model for sand. *GÃ©otechnique Letters* **9**, No. 2, 81–88, doi: 10.1680/jgele.18.00187.

Liu, H. Y., Zygounas, F., Diambra, A. & Pisanò, F. (2018). Enhanced plasticity modelling of high-cyclic ratcheting and pore pressure accumulation in sands. In *Numerical methods in geotechnical engineering IX, volume 1: proceedings of the 9th European conference on numerical methods in geotechnical engineering (NUMGE 2018)*, CRC Press/Balkema Leiden, the Netherlands, pp. 87–96.

Nemat-Nasser, S. & Tobita, Y. (1982). Influence of fabric on liquefaction and densification potential of cohesionless sand. *Mechanics of Materials* **1**, No. 1, 43–62.

Downloaded by [NORGES GEOTEKNISKE INSTITUTT] on [29/10/21]. Copyright © ICE Publishing, all rights reserved.

Accepted manuscript doi:
10.1680/jgeot.21.00068

Papadimitriou, A. G., Chaloulos, Y. K. & Dafalias, Y. F. (2019). A fabric-based sand plasticity model with reversal surfaces within anisotropic critical state theory. *Acta Geotechnica* **14**, No. 2, 253–277.

Petalas, A. L., Dafalias, Y. F. & Papadimitriou, A. G. (2019). Sanisand-fn: An evolving fabric-based sand model accounting for stress principal axes rotation. *International Journal for Numerical and Analytical Methods in Geomechanics* **43**, No. 1, 97–123.

Pisanò, F. (2019). Input of advanced geotechnical modelling to the design of offshore wind turbine foundations. In *Proceedings of the 17th European Conference on Soil Mechanics and Geotechnical Engineering (ECSMGE 2019)*, International Society of Soil Mechanics and Geotechnical Engineering.

Richards, I., Bransby, M., Byrne, B., Gaudin, C. & Houlsby, G. (2021). Effect of stress level on response of model monopile to cyclic lateral loading in sand. *Journal of Geotechnical and Geoenvironmental Engineering* **147**, No. 3, 04021002.

Richards, I. A., Byrne, B. W. & Houlsby, G. T. (2020). Monopile rotation under complex cyclic lateral loading in sand. *Géotechnique* **70**, No. 10, 916–930.

Sloan, S. W. (1987). Substepping schemes for the numerical integration of elastoplastic stress–strain relations. *International journal for numerical methods in engineering* **24**, No. 5, 893–911.

Sun, J. I., Golesorkhi, R. & Seed, H. B. (1988). *Dynamic moduli and damping ratios for cohesive soils*. Earthquake Engineering Research Center, University of California Berkeley.

Tasiopoulou, P., Chaloulos, Y., Gerolymos, N., Giannakou, A. & Chacko, J. (2021). Cyclic lateral response of owt bucket foundations in sand: 3d coupled effective stress analysis with ta-ger model. *Soils and Foundations* .

Truong, P., Lehane, B. M., Zania, V. & Klinkvort, R. T. (2019). Empirical approach based on centrifuge testing for cyclic deformations of laterally loaded piles in sand. *Géotechnique* **69**, No. 2, 133–145, doi: 10.1680/jgeot.17.P.203.

Wichtmann, T. & Triantafyllidis, T. (2016). An experimental database for the development, calibration and verification of constitutive models for sand with focus to cyclic loading: part i-tests with monotonic loading and stress cycles. *Acta Geotechnica* **11**, No. 4, 739–761.

Ziotopoulou, K. (2018). Seismic response of liquefiable sloping ground: Class a and c numerical predictions of centrifuge model responses. *Soil dynamics and earthquake engineering* **113**, 744–757.

Table 1. SANISAND-MSu parameters for Karlsruhe fine sand tested by Wichtmann & Triantafyllidis (2016)

G_0	ν	M	c	λ_c	e_0	ξ	m	h_0	c_h
95	0.05	1.35	0.81	0.55	1.035	0.36	0.01	7.6	0.97
n^b	A_0	n^d	β_1	β_2	k	μ_0	ζ	w_1	w_2
1.2	0.74	1.79	4	3.2	2	65	0.0003	2.5	1.5

Downloaded by [NORGES GEOTEKNISKE INSTITUTT] on [29/10/21]. Copyright © ICE Publishing, all rights reserved.

Accepted manuscript doi:
10.1680/jgeot.21.00068

Figure captions

Figure 1. SANISAND-MSu model in stress ratio $\boldsymbol{\pi}$ plane.

Figure 2. Stress controlled undrained cyclic DSS tests. Simulation results using (a) SANISAND2004 model and (b) SANISAND-MSu model. Simulation conditions : D_r =65%, $\sigma_{v0} = 100$ kPa, $\tau^{ampl} = 15$ kPa.

Figure 3. Stress controlled undrained cyclic triaxial test: comparison between experimental data (Wichtmann & Triantafyllidis, 2016) and SANISAND-MSu simulation results. Simulation/test conditions: (a)-(d): $p_{in} = 200$ kPa, $q^{ampl} = 50$ kPa, $D_r = 65\%$; (e)-(h): $p_{in} = 300$ kPa, $q^{ampl} = 75$ kPa, $D_r = 64\%$. Simulation results modified after Liu *et al*. (2020).

Figure 4. Pore water pressure ratio against number of loading cycles on medium dense sand ($D_r = 65\%$): comparison between experimental data (Wichtmann & Triantafyllidis, 2016) and SANISAND-MSu simulation results.

Figure 5. Effects of: (a) initial vertical stress σ_{v0} and (b) relative density D_r on stiffness degradation curves: SANISAND-MSu model simulation results compared with empirical equation proposed by Darendeli (2001) and Sun *et al*. (1988).

Figure 6. Definition of damping.

Figure 7. Damping ratio curves obtained from SANISAND-MSu model. Simulation conditions: stress controlled undrained cyclic DSS tests, stress-strain response in cyclic mobility stage included.

Figure 8. FE model domain.

Figure 9. Behaviour of monopile subjected to the first symmetric loading cycle: (a) results of centrifuge tests in dry sand (Richards *et al*., 2021) (b) 3D FE analysis results in both drained and undrained sand: comparison between SANISAND-MSu and SANISAND2004 results.

Figure 10. Distribution of $\boldsymbol{p} / p_{in}$ ratio in sand domain during the first loading cycle.

Figure 11. Pile force displacement response in (a) undrained and (b) drained sand. Symmetrical horizontal load applied at pile head.

Figure 12. Distribution of excess pore water pressure in soil after 10 cycles ($\boldsymbol{H} = 0$) in undrained soil.

Figure 13. Pile deformation against loading cycles in (a) undrained sand and (b) drained sand.

Figure 14. Pile reaction force: comparison between undrained and drained simulation results using SANISAND-MSu 3D FE. Results for different loading cycles $\boldsymbol{N}$ at $\boldsymbol{H} = H_{max}$.

Figure 15. Pile shear force and bending moment: comparison between undrained and drained simulation results using SANISAND-MSu 3D FE. Results for different loading cycles N at $\boldsymbol{H} = H_{max}$.

Figure 16. Soil resistance against pile displacement - comparison between undrained and drained simulation results using SANISAND-MSu 3D FE. Pile response is at depth $\boldsymbol{z} = 2.5D_{pile}$ and $0.3D_{pile}$ respectively.

Downloaded by [NORGES GEOTEKNISKE INSTITUTT] on [29/10/21]. Copyright © ICE Publishing, all rights reserved.

Accepted manuscript doi:
10.1680/jgeot.21.00068

Figure 17. Stress paths in $\frac{\tau_{xz}}{\boldsymbol{p}} \sim \frac{\sigma_z - \sigma_x}{2\boldsymbol{p}}$ plane for representative elements (see Fig. 8).

Figure 18. $\boldsymbol{q} \sim \boldsymbol{p}$ response and $\boldsymbol{\tau} \sim \boldsymbol{\gamma}$ response for representative elements (see Fig. 8).

Figure 19. Evolution of pore water pressure ratio against number of loading cycles: (a) load level same as in Fig. 9 to Fig. 18; (b) load reduced to half of case (a).

Downloaded by [NORGES GEOTEKNISKE INSTITUTT] on [29/10/21]. Copyright © ICE Publishing, all rights reserved.

Accepted manuscript doi:
10.1680/jgeot.21.00068

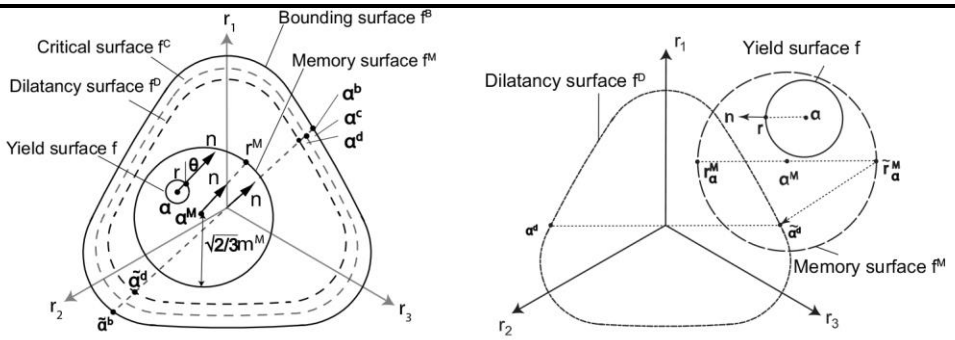

(a) Relevant model loci/tensors

(b) Components for dilatancy coeffcient A_d

Fig. 1

Downloaded by [NORGES GEOTEKNISKE INSTITUTT] on [29/10/21]. Copyright © ICE Publishing, all rights reserved.

Accepted manuscript doi:
10.1680/jgeot.21.00068

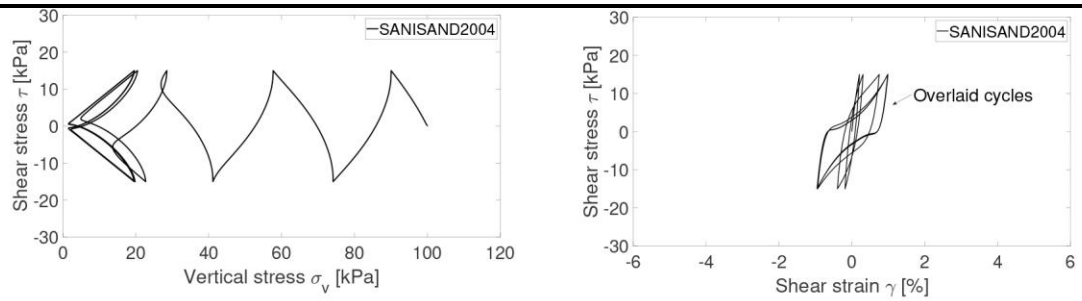

(a) SANISAND2004, $z_{max} = 4$, $c_z = 400$

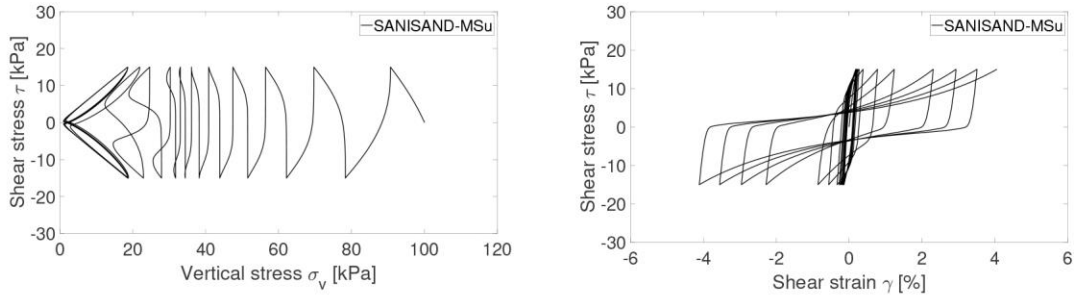

(b) SANISAND-MSu, model parameters as listed in Table 1.

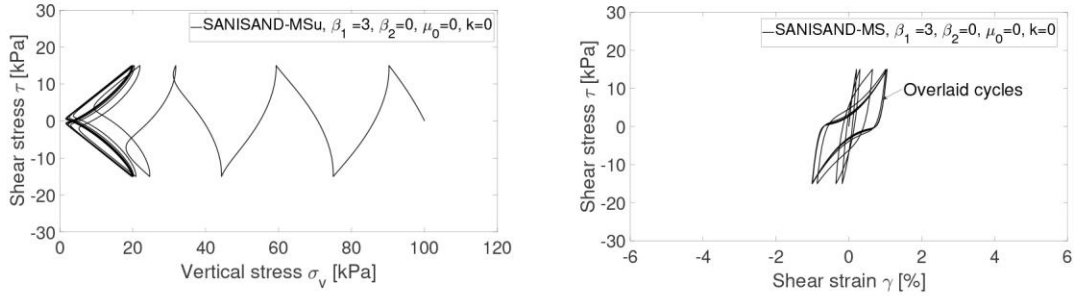

(c) SANISAND-MSu, β_1=3, β_2=0, μ_0=0, k=0. Other parameters as listed in Table 1

Fig. 2

Downloaded by [NORGES GEOTEKNISKE INSTITUTT] on [29/10/21]. Copyright © ICE Publishing, all rights reserved.

Accepted manuscript doi:
10.1680/jgeot.21.00068

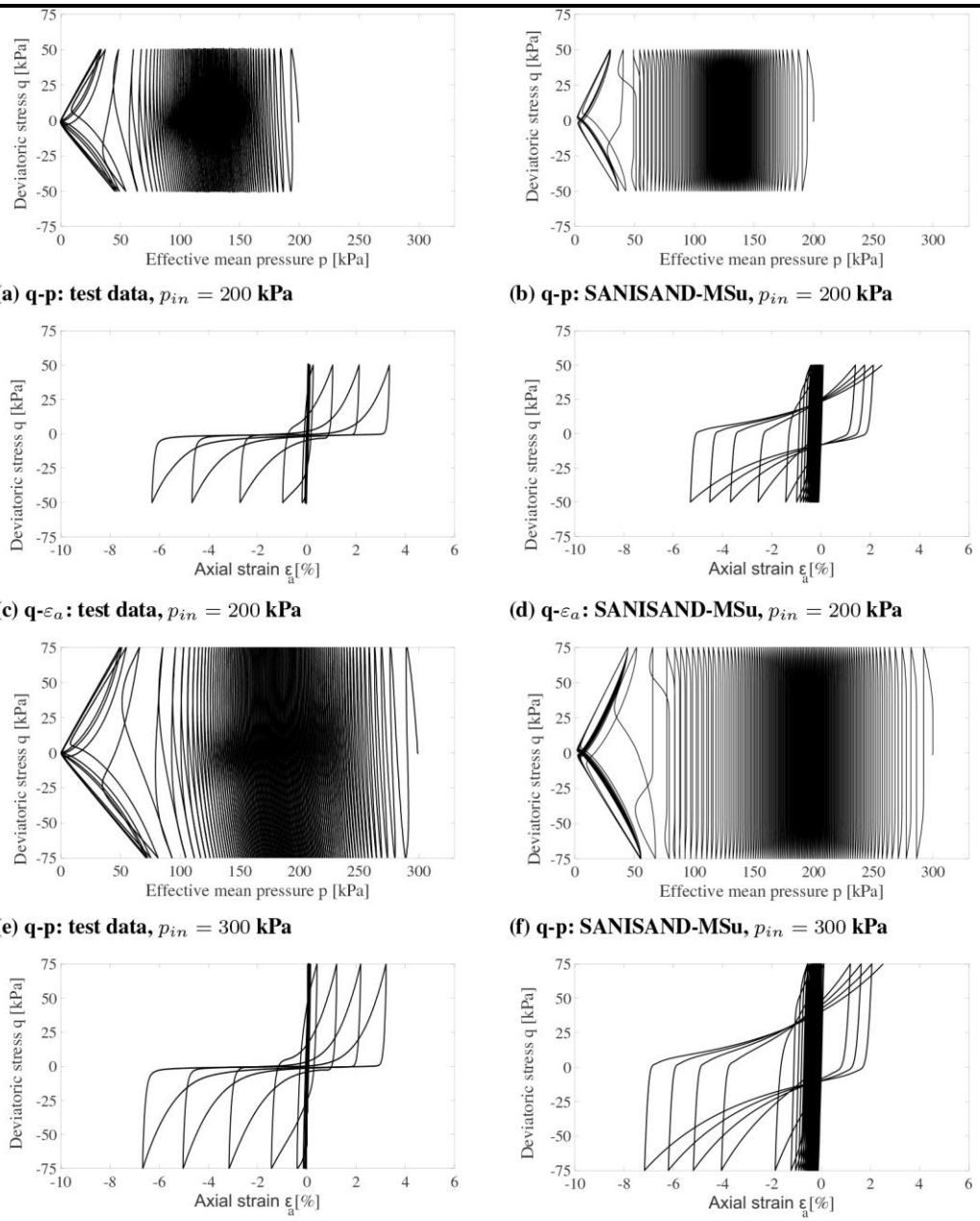

(a) q-p: test data, $p_{in} = 200$ **kPa**

(b) q-p: SANISAND-MSu, $p_{in} = 200$ **kPa**

(c) q-ε_a: test data, $p_{in} = 200$ **kPa**

(d) q-ε_a: SANISAND-MSu, $p_{in} = 200$ **kPa**

(e) q-p: test data, $p_{in} = 300$ **kPa**

(f) q-p: SANISAND-MSu, $p_{in} = 300$ **kPa**

(g) q-ε_a: test data, $p_{in} = 300$ **kPa**

(h) q-ε_a: SANISAND-MSu, $p_{in} = 300$ **kPa**

Fig. 3

Downloaded by [NORGES GEOTEKNISKE INSTITUTT] on [29/10/21]. Copyright © ICE Publishing, all rights reserved.

Accepted manuscript doi:
10.1680/jgeot.21.00068

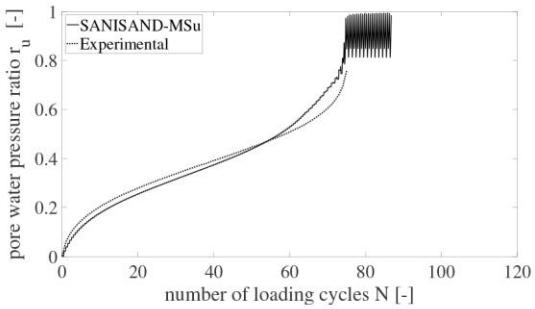

(a) $p_{in} = 200$ **kPa,** $q^{ampl} = 50$ **kPa**

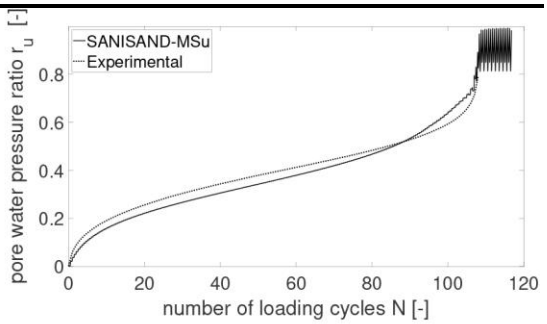

(b) $p_{in} = 300$ **kPa,** $q^{ampl} = 75$ **kPa**

Fig. 4

Downloaded by [NORGES GEOTEKNISKE INSTITUTT] on [29/10/21]. Copyright © ICE Publishing, all rights reserved.

Accepted manuscript doi:
10.1680/jgeot.21.00068

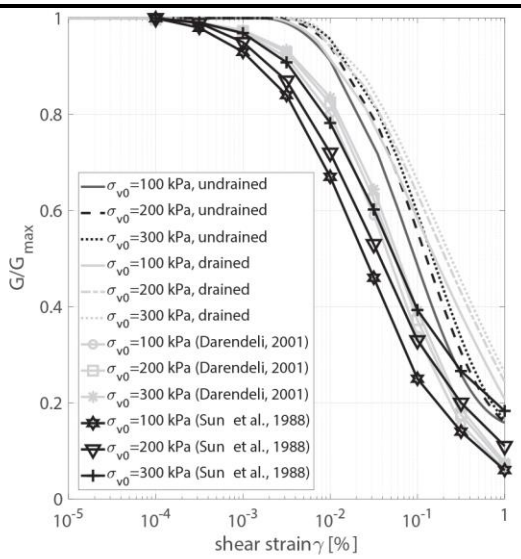

(a) $D_r = 80\%$.

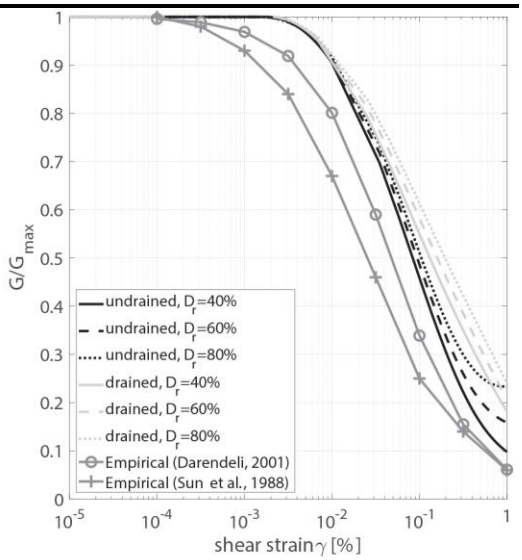

(b) σ_{v0}**=200 kPa**

Fig. 5

Downloaded by [NORGES GEOTEKNISKE INSTITUTT] on [29/10/21]. Copyright © ICE Publishing, all rights reserved.

Accepted manuscript doi:
10.1680/jgeot.21.00068

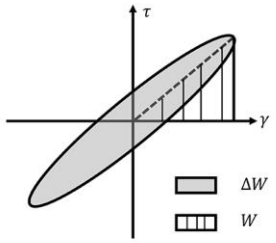

Fig. 6

Downloaded by [NORGES GEOTEKNISKE INSTITUTT] on [29/10/21]. Copyright © ICE Publishing, all rights reserved.

Accepted manuscript doi:
10.1680/jgeot.21.00068

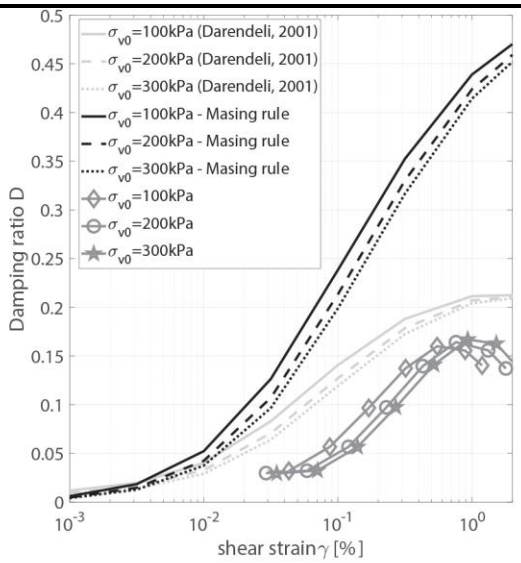

(a) Effects of initial vertical stress σ_{v0}.

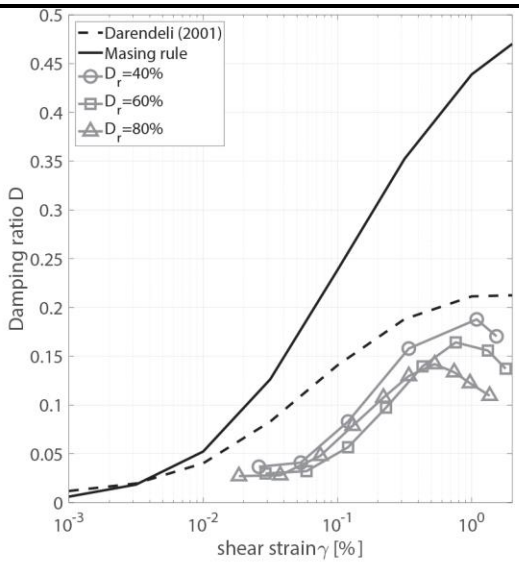

(b) Effects of relative density D_r.

Fig. 7

Downloaded by [NORGES GEOTEKNISKE INSTITUTT] on [29/10/21]. Copyright © ICE Publishing, all rights reserved.

Accepted manuscript doi:
10.1680/jgeot.21.00068

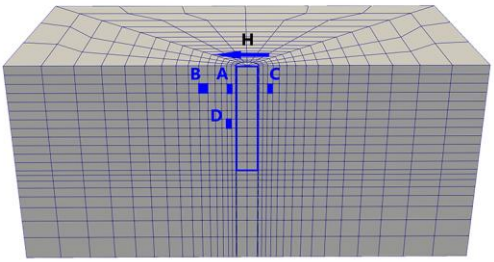

Fig. 8

Downloaded by [NORGES GEOTEKNISKE INSTITUTT] on [29/10/21]. Copyright © ICE Publishing, all rights reserved.

Accepted manuscript doi:
10.1680/jgeot.21.00068

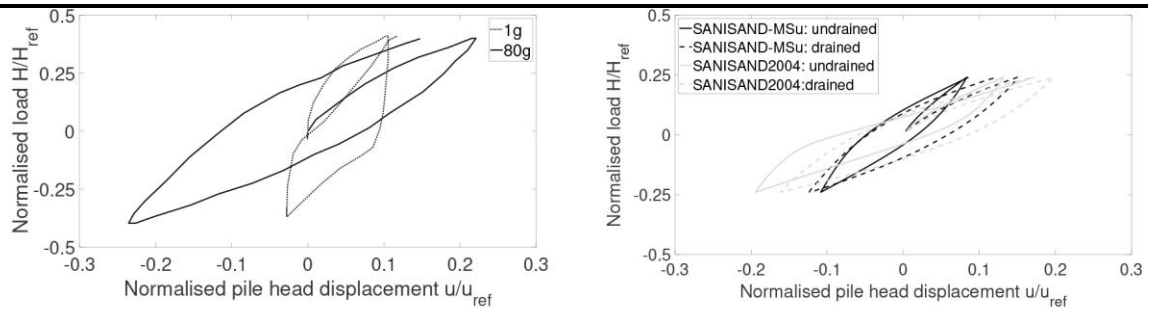

(a) $H/H_{ref} = 0.4$ **(Richards *et al.*, 2021)** **(b)** $H/H_{ref} = 0.24$ **(FE results)**

Fig. 9

Downloaded by [NORGES GEOTEKNISKE INSTITUTT] on [29/10/21]. Copyright © ICE Publishing, all rights reserved.

Accepted manuscript doi:
10.1680/jgeot.21.00068

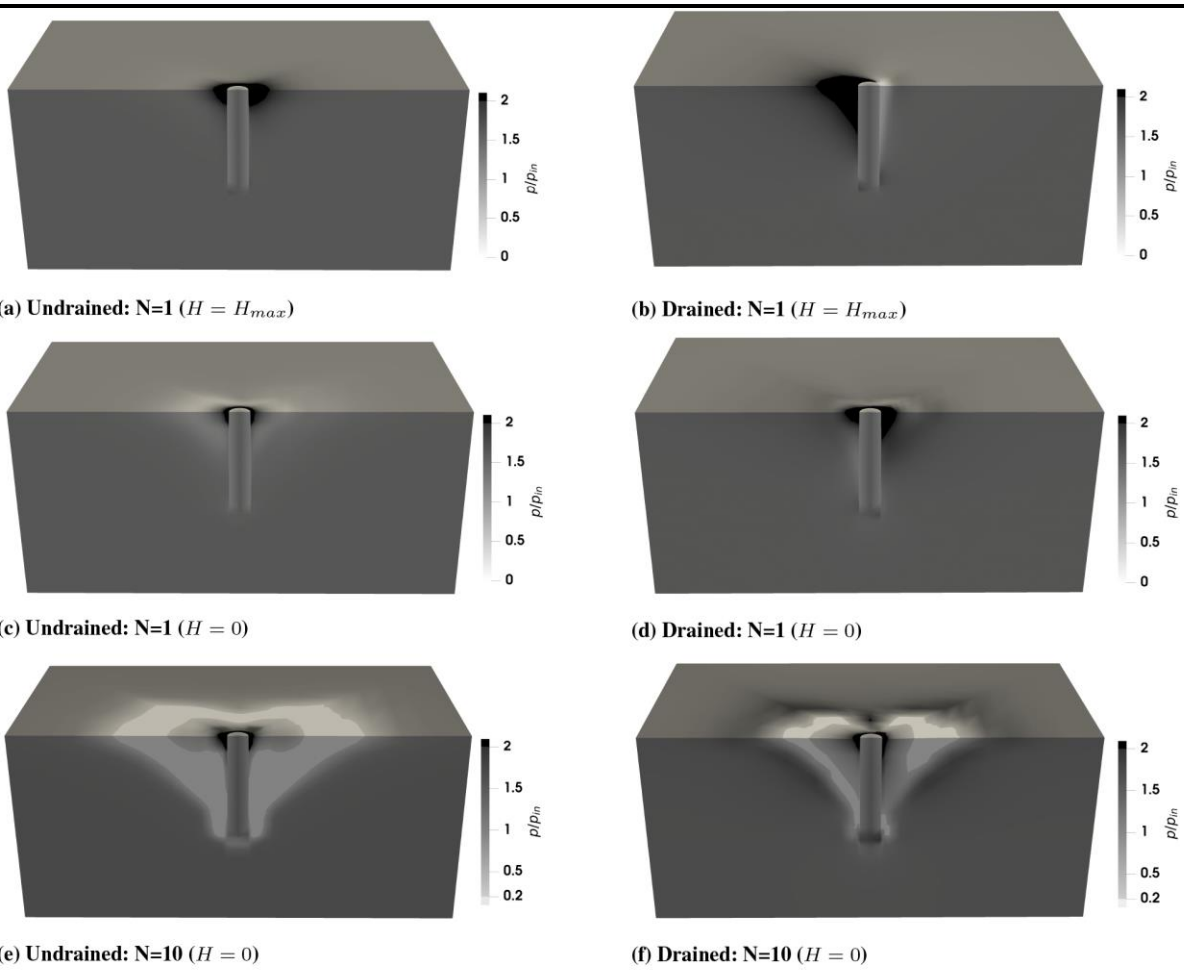

(a) Undrained: N=1 ($H = H_{max}$)

(b) Drained: N=1 ($H = H_{max}$)

(c) Undrained: N=1 ($H = 0$)

(d) Drained: N=1 ($H = 0$)

(e) Undrained: N=10 ($H = 0$)

(f) Drained: N=10 ($H = 0$)

Fig. 10

Downloaded by [NORGES GEOTEKNISKE INSTITUTT] on [29/10/21]. Copyright © ICE Publishing, all rights reserved.

Accepted manuscript doi:
10.1680/jgeot.21.00068

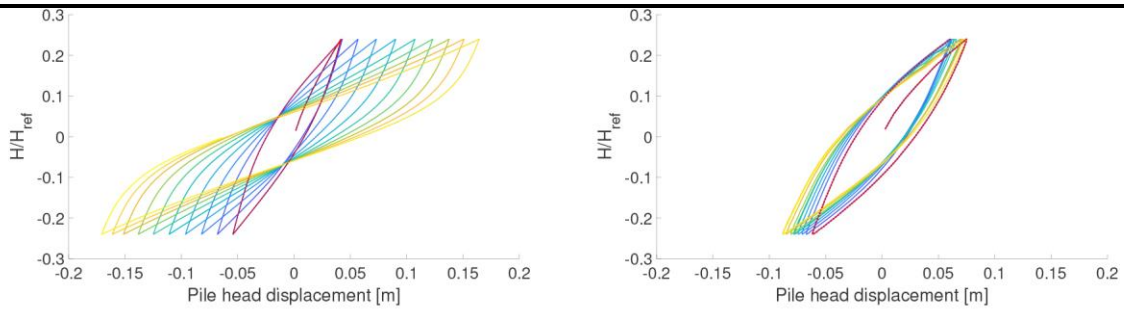

(a) Undrained **(b) Drained**

Fig. 11

Downloaded by [NORGES GEOTEKNISKE INSTITUTT] on [29/10/21]. Copyright © ICE Publishing, all rights reserved.

Accepted manuscript doi:
10.1680/jgeot.21.00068

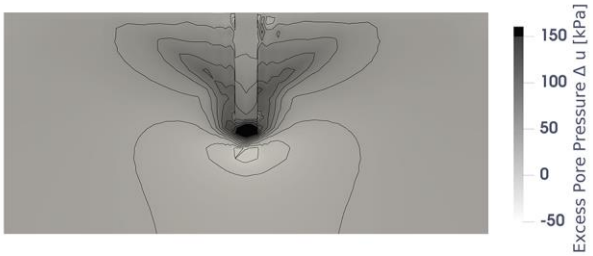

Fig. 12

Downloaded by [NORGES GEOTEKNISKE INSTITUTT] on [29/10/21]. Copyright © ICE Publishing, all rights reserved.

Accepted manuscript doi:
10.1680/jgeot.21.00068

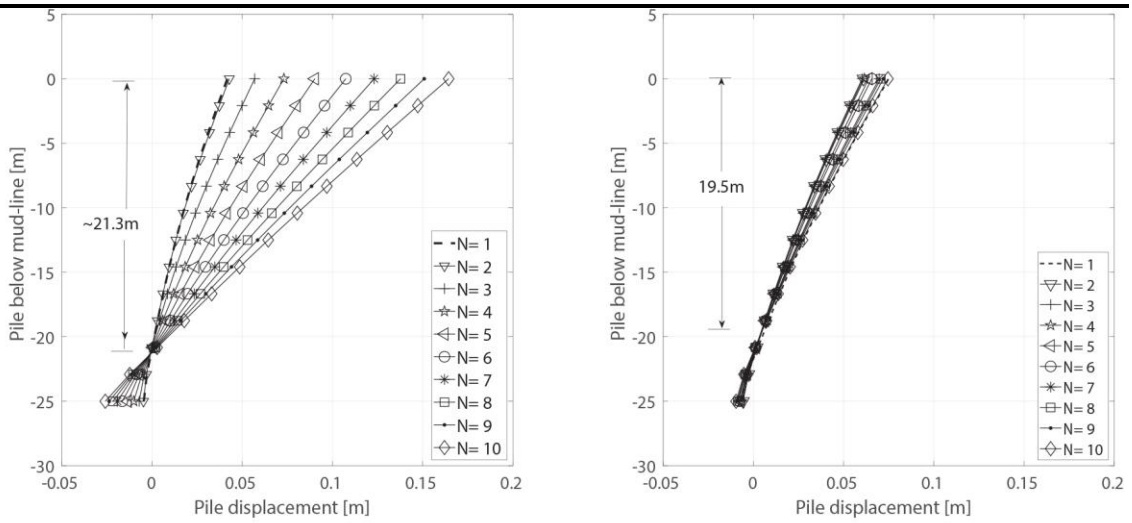

(a) Undrained **(b) Drained**

Fig. 13

Downloaded by [NORGES GEOTEKNISKE INSTITUTT] on [29/10/21]. Copyright © ICE Publishing, all rights reserved.

Accepted manuscript doi:
10.1680/jgeot.21.00068

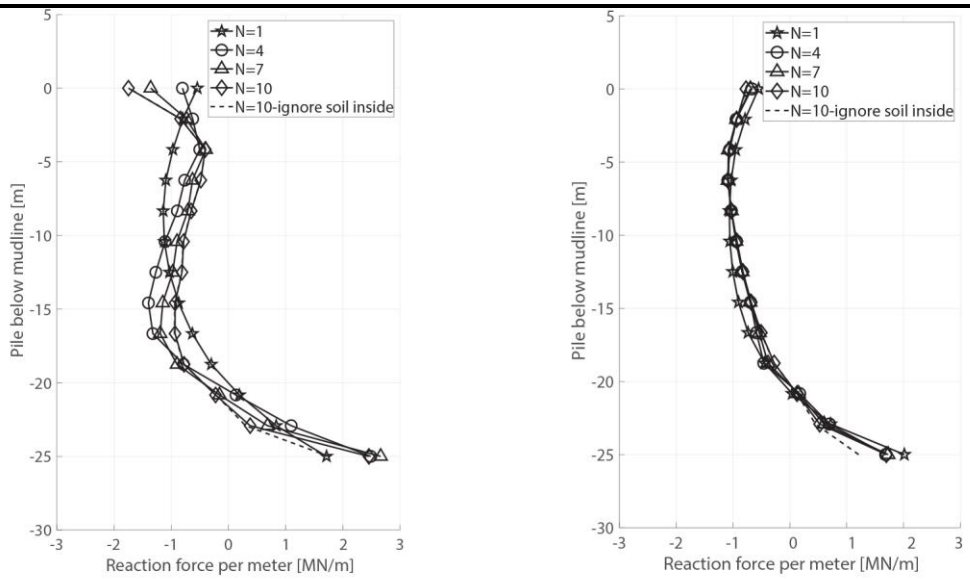

(a) Undrained **(b) Drained**

Fig. 14

Downloaded by [NORGES GEOTEKNISKE INSTITUTT] on [29/10/21]. Copyright © ICE Publishing, all rights reserved.

Accepted manuscript doi:
10.1680/jgeot.21.00068

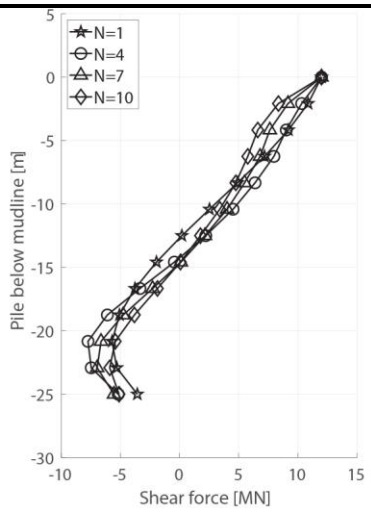

(a) Shear force: undrained

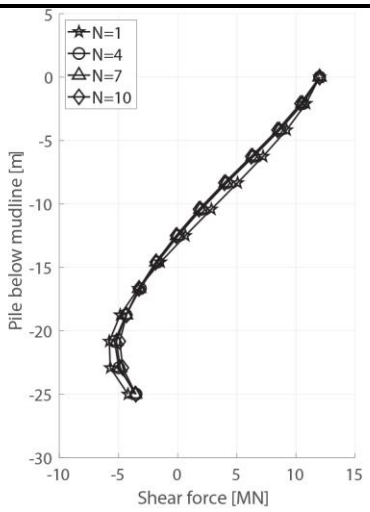

(b) Shear force: drained

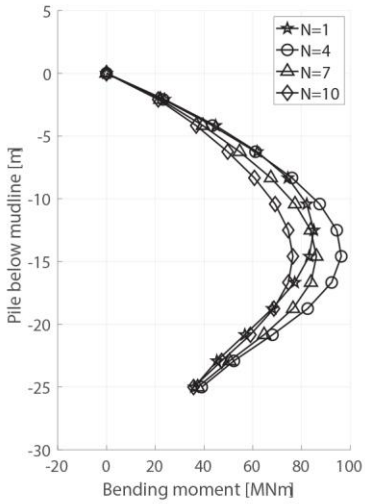

(c) Bending moment: undrained

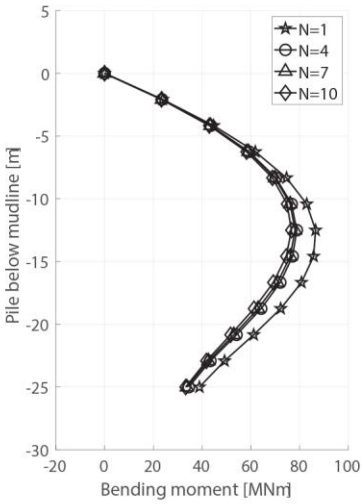

(d) Bending moment: drained

Fig. 15

Downloaded by [NORGES GEOTEKNISKE INSTITUTT] on [29/10/21]. Copyright © ICE Publishing, all rights reserved.

Accepted manuscript doi:
10.1680/jgeot.21.00068

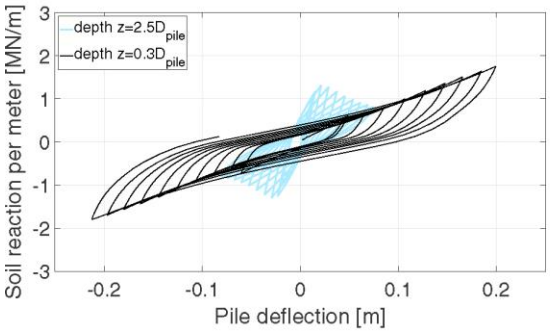

(a) Undrained

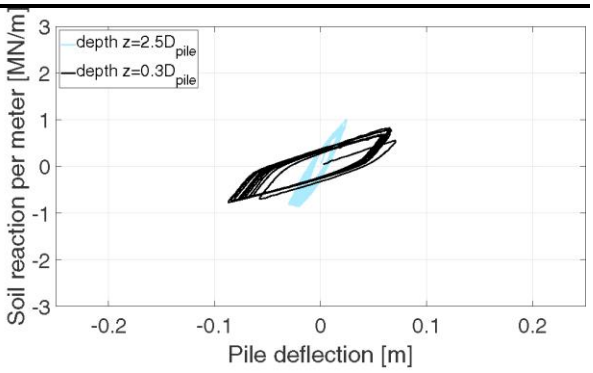

(b) Drained

Fig. 16

Downloaded by [NORGES GEOTEKNISKE INSTITUTT] on [29/10/21]. Copyright © ICE Publishing, all rights reserved.

Accepted manuscript doi:
10.1680/jgeot.21.00068

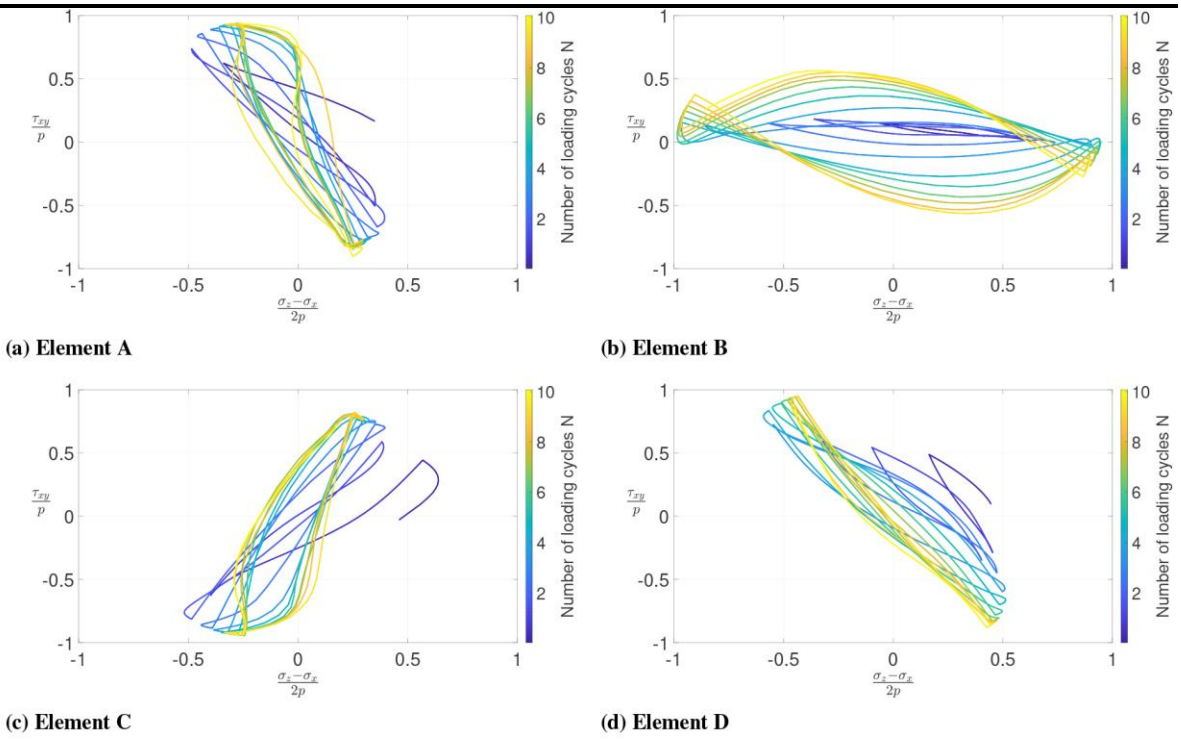

(a) Element A

(b) Element B

(c) Element C

(d) Element D

Fig. 17

Downloaded by [NORGES GEOTEKNISKE INSTITUTT] on [29/10/21]. Copyright © ICE Publishing, all rights reserved.

Accepted manuscript doi:
10.1680/jgeot.21.00068

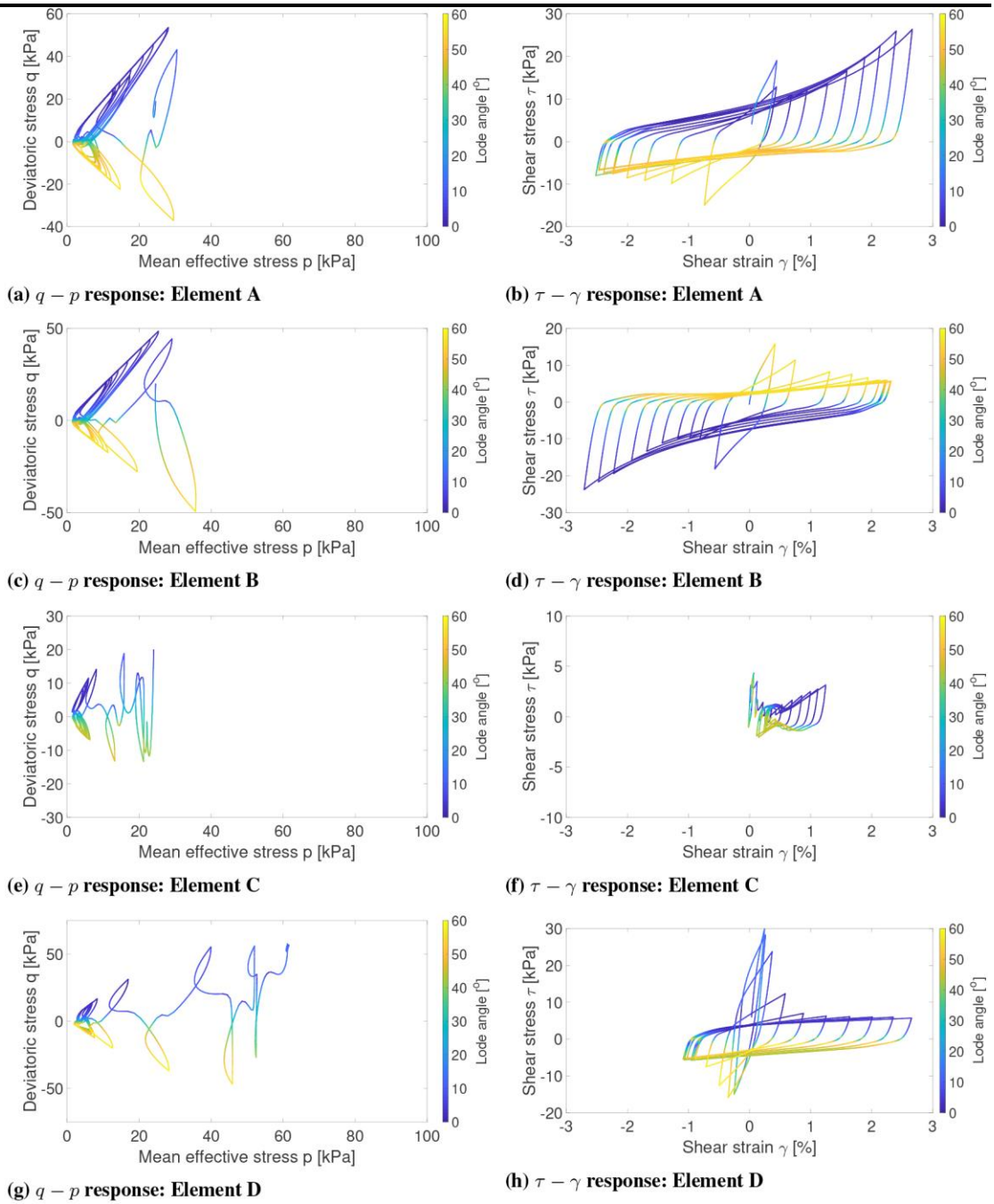

(a) $q - p$ **response: Element A**

(b) $\tau - \gamma$ **response: Element A**

(c) $q - p$ **response: Element B**

(d) $\tau - \gamma$ **response: Element B**

(e) $q - p$ **response: Element C**

(f) $\tau - \gamma$ **response: Element C**

(g) $q - p$ **response: Element D**

(h) $\tau - \gamma$ **response: Element D**

Fig. 18

Downloaded by [NORGES GEOTEKNISKE INSTITUTT] on [29/10/21]. Copyright © ICE Publishing, all rights reserved.

Accepted manuscript doi:
10.1680/jgeot.21.00068

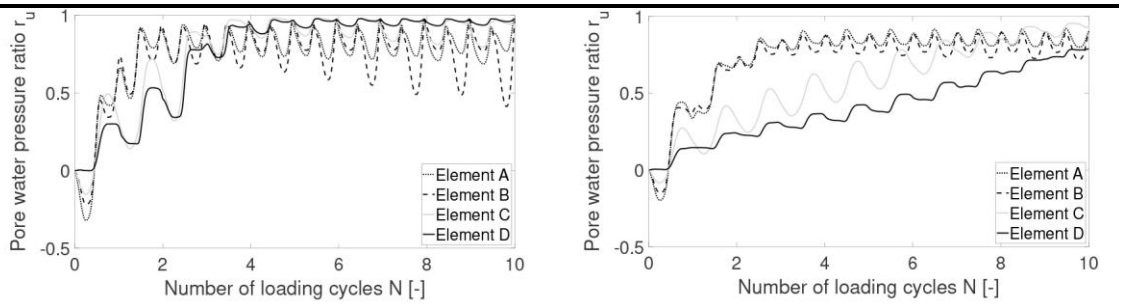

Fig. 19

Downloaded by [NORGES GEOTEKNISKE INSTITUTT] on [29/10/21]. Copyright © ICE Publishing, all rights reserved.